The plasma properties of laser-ablated SiO_2

Paul J. Wolf
Frank J. Seiler Research Laboratory, U.S. Air Force Academy, Colorado 80840-6528

(Received 7 February 1992; accepted for publication 30 April 1992)

The optical emission from laser-produced plasmas generated by 1.06 μm irradiation of SiO_2 targets at a flux of 7×10^{10} W cm^{-2} was recorded and analyzed between 250 and 800 nm. The ionization states of Si and O were mapped as a function of both time from the incident laser pulse and location from the front surface of the target. Electron temperatures were calculated using the relative emission intensities of Si(II) and O(II) ionization states ($T_e=3.4$ eV), and an electron number density was determined from the Stark-broadened linewidths of five Si(II) emission lines. The ablated material was collected on Si substrates to examine the particulate nature of the plasma. Thin films were grown in the process and properties of these films were examined using IR reflectance and transmittance spectroscopy, scanning electron microscope analyses, and Auger electron spectroscopy.

ODUCTION

When a pulsed laser of sufficiently high flux ϕ, is focused onto the surface of a target, the material beneath the focused laser spot can rapidly reach its vaporization temperature whereupon small amounts of target material can be ejected into the surrounding medium. The interaction of the laser with the target material involves complex processes which depend on the properties of both the laser (power density, pulse duration, and wavelength) and the solid (thermodynamics and optical properties). Generally, surface melting and material evaporation results in the formation of neutral atoms, molecules, and cluster species for incident laser fluxes, $\phi<10^6$ W cm^{-2}. For fluxes, $\phi\geqslant10^8$ W cm^{-2}, the vaporized species include fast and electronically excited neutral atoms, molecules, ions, and electrons. This particular flux regime is usually characterized by the formation of a plasma. If the ablation is performed in a vacuum, the plasma's behavior is governed by gas dynamic processes on the nanosecond time scale. The production and nature of laser-produced plasmas (LPP) is itself an interesting field of study since modeling these events is rather difficult. Therefore, obtaining information on the characteristics of these plasmas will provide details for a clearer understanding of this phenomena.

The study of laser-produced plasmas is intrinsically interesting, but it also has important practical applications. The material ejected from a target exposed to a high-flux laser carries both mass and energy that can be used to form thin films. The physical characteristics of the ejecta play a crucial role in the microscopic mechanism of film growth.[1] Pulsed laser deposition (PLD) is, indeed, one of many popular methods employed to fabricate thin films.[2] Generally, PLD is useful for forming multicomponent films from targets that are stoichiometrically complex and the method is employed for targets with high vaporization temperatures. It is believed that the structure of thin films depends largely on the deposition process.[3,4] For example, laser-ablated materials consisting of ions and excited species impact the film growth surface at energies that may enhance surface diffusion of adsorbed atoms to improve the film's structural properties. By determining the energy and mass content of the laser-ablated material and correlating the plasma conditions with the film properties, one may be able to optimize the deposition conditions for choice films. However, despite many accounts found in the current literature on film production using PLD, only a few studies report detailed analyses of the laser-vaporized material used in the film deposition process.[5-8]

Both the thermal and optical properties of the target material determine the choice of the laser. Previous studies on dielectric material laser ablation utilized CO_2 or ruby lasers to achieve a plasma because the chosen target materials are highly absorbing at these wavelengths.[1] These wavelengths also afford flux tunability so the phenomena can be studied at various laser conditions. At high power densities, however, all materials become absorbing to some degree to any wavelength due to surface breakdown and plasma formation.[9,10] In this study, a luminescent plasma was generated by surface breakdown on a SiO_2 target using a Nd:YAG laser at high power densities. The readily observable optical emission from this LPP was diagnosed using optical emission spectroscopy,[11,12] and information about the ionic character of the plasma was extracted. Numerous excited neutral and ionized species were identified, and the temperature of the plasma was deduced from the measured spectroscopic line intensities under the assumption of local thermodynamic equilibrium (LTE). In order to verify that the results indeed justify the initial LTE assumption, theoretical self-consistency checks are presented in Sec. IV. The plasma material was also collected on silicon substrates to examine the particulate nature of the blowoff. Films were generated in the process and bulk properties of these films were determined using several film diagnostic techniques.

II. EXPERIMENT

The experimental arrangement is illustrated in Fig. 1. The ablation experiments were performed in a stainless-steel vacuum chamber which typically achieved a base pressure of 5×10^{-7} Torr using a cryopump (CTI Cryo-

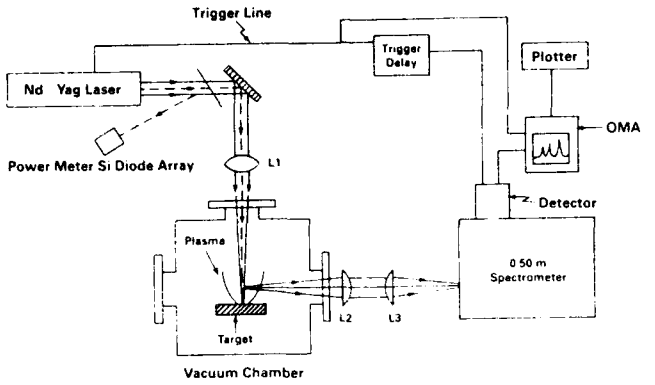

FIG. 1. Schematic diagram of the experimental apparatus.

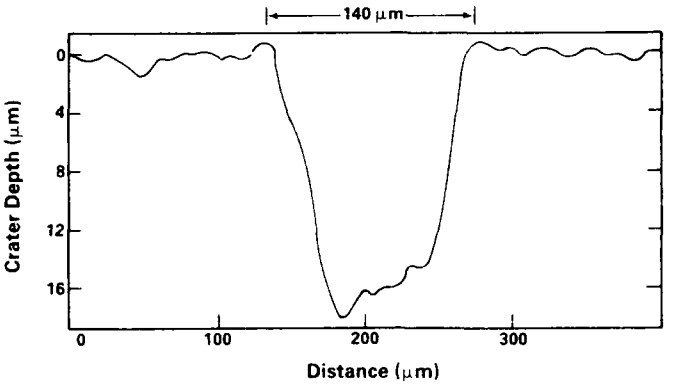

FIG. 2. Depth profile of a crater produced after one laser pulse on a SiO_2 target. The energy on target was 230 mJ.

genics CT-100). A Q-switched Nd:YAG laser (Quanta-Ray DCR 2), which produced 1.06 μm radiation in 10 ns [full width at half-maximum (FWHM)] pulse widths, was focused (lens L1) onto the surface of a 99.99% pure SiO_2 target. The output energy of the laser was 250 mJ/pulse and the laser energy was constant to within 5% from shot to shot as measured with a Scientech 350 energy meter. The energy on target was approximately 90% of the total laser energy due to losses from both the turning optics and the entrance window on the vacuum chamber. Since SiO_2 is nonabsorbing at 1.06 μm, high laser fluxes were required to achieve breakdown near the target surface.[10] The high flux was obtained using a tightly focused laser at constant energy. Typically, the focused beam was approximately 120 μm in diameter which generated a laser flux of 7×10^{10} W cm^{-2}. (The spatial width of the focused laser beam was measured by recording the laser footprint with a 1024 element linear silicon diode array.) Plasma production was extremely sensitive to the laser fluence. A factor of 2 reduction in the fluence extinguished the plasma emission which indicated that the experiment was operating near plasma threshold. Thus, all the data in this study were obtained at one laser flux.

The craters formed on the target by the focused laser were characterized using a Tencor Alpha Step 200 surface profiler. A typical crater profile from a single 230 mJ laser pulse is shown in Fig. 2. The diameter of the crater obtained from such profiles, $\simeq 140$ μm, was in good agreement with the laser-beam profile measurement obtained using the Si diode array. These crater depth measurements were useful for estimating the amount of material ablated from the target. The approximate volume of the crater shown in Fig. 2 is 2.5×10^{-7} cm^3. Since SiO_2 has a mass density of 2.65 g cm^{-3}, approximately 0.66 μg of material was removed from the target in a single laser shot.

The target was mounted on a precision y-z translation stage inside the vacuum chamber. The y-axis adjustment accessed unexposed target material to the laser while the z-axis adjustment allowed positional variation of the target relative to the image collection system. By adjusting the target along the z axis, plasma emission data were recorded as a function of distance z from the front of the target surface. The z-axis travel, however, was limited to 1 cm from the front of the target, and the $z=0$ plane was identified as the position where all emission disappeared.

The plasma emission was imaged approximately 1:1 by two quartz, aspheric lenses (L2 and L3) onto the entrance slits of a 0.5 m spectrometer which had an instrumental resolution of 0.17 nm. The reciprocal linear dispersion of the grating was 1.66 nm/mm which allowed 20 nm of optical information to be collected in a single shot. The dispersed emission was subsequently detected by a 10 ns, gated, image-intensified optical multichannel analyzer (PAR OMA III). Five laser shots usually provided data with an adequate signal-to-noise ratio. The temporal history of the plasma was obtained by recording the emission features at predetermined delay times using a variable delay generator which was triggered by the laser pulse.

The spectral sensitivity of the spectrometer-OMA III system was calibrated using a quartz-halogen lamp (Optronic Laboratories, Inc. Model 345-RP). A calibration curve was developed by determining the relative intensity in a specific spectral region and comparing these measurements with the manufacturer's published values. The ratio of these two relative intensities defined a calibration factor for each wavelength region. The spectral response correction was calculated in 20 nm segments, so there was an about a 35% uncertainty in comparing line intensities between different figures. The wavelength indicator on the spectrometer was also calibrated from 250 to 800 nm using an assortment of spectral lamps. The wavelength error was ±0.2 nm.

The products of the laser-produced plasma were collected on Si substrates to examine the particulate nature of the laser-ablated material. Thin films were also grown during the collection process. These experiments were conducted in a separate vacuum chamber under identical laser and vacuum conditions as that used in the plasma emission experiments. The laser was focused to $\simeq200$ μm in diameter and intersected the target at approximately 27° with respect to the target-substrate axis, unlike the normal incidence used in the plasma emission studies. The substrates were placed 3 and 6 cm from the target and they were not pretreated before the film deposition. Several deposition times were also employed in these studies. A thermocouple

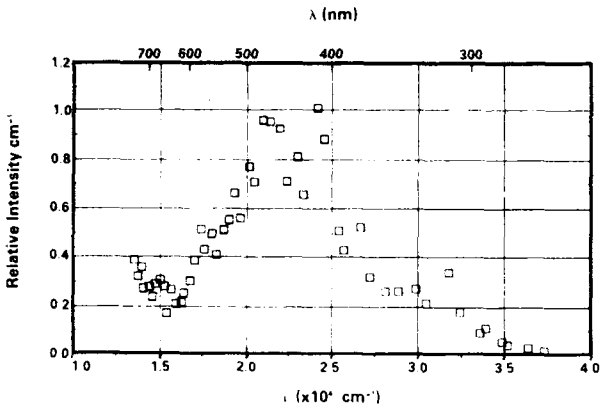

FIG. 3. Continuum emission intensity of a plasma generated at $\phi = 7 \cdot 10^{10}$ W cm^{-2}. The data were recorded at 1.1 mm from the target surface and 30 ns into the plasma development.

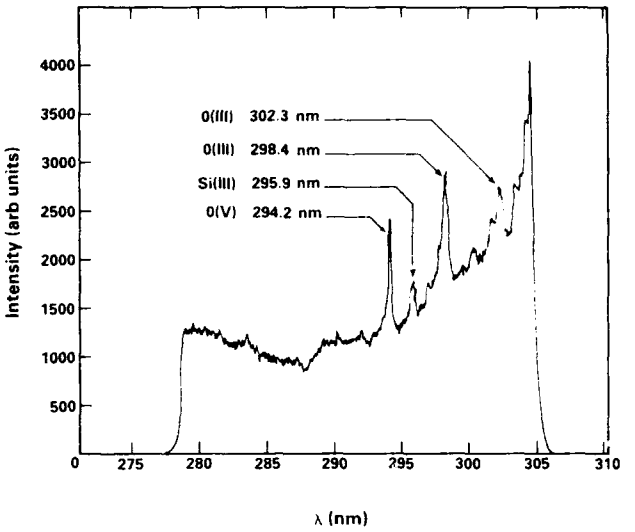

FIG. 4. The continuum background at $z = 1.5$ mm and $t_d = 30$ ns showing the appearance of line emission from the $+3$ and $+4$ ionization stages of O and Si. The emission was not corrected for its spectral response; consequently, the emission spectrum appears to increase in intensity toward longer wavelengths where the detection system becomes more efficient.

was attached to the substrate holder to detect any changes in the substrate temperature during the collection of the ablated material. The target was also rotated during the ablation to prevent crater formation in a single location. The bulk properties of the films were diagnosed using the surface profiler, a scanning electron microscope (SEM), Auger spectroscopy for surface composition, and IR reflectance and transmittance spectroscopy.

III. RESULTS

A. Plasma emission

The plasma emission spectrum was recorded at several distances z from the target surface and at different delay times t_d in the wavelength region 250 nm$\leqslant\lambda\leqslant$800 nm. An intense continuum close to the target surface was observed in the initial stage of the plume development. This emission was attributed to both elastic collisions of electrons with ions and atoms (free-free emission) and the recombination of electrons with ions (free-bound emission).[13] Figure 3 shows the relative intensity of the continuum emission versus wavelength recorded at 1.1 mm from the target surface and approximately 30 ns into the plasma evolution. The continuum intensity exhibited a maximum between 400 and 500 nm with a gradual reduction towards zero near 250 nm. The curve also indicated a minimum near 700 nm but the cause is not fully understood. However, this minimum does approximately correspond to the energy difference required in the electron-ion recombination of Si(II) to form Si(I)* in the $3p^3\,{}^3D^0$ state which resides 5440 cm^{-1} above the first electronically excited state of Si(I).

Line emission dominated the radiation process as the plasma cooled and expanded away from the target. The first discrete emission lines appeared near the target surface (superimposed on the continuum) and originated from primarily doubly and triply ionized states of O and Si. Figure 4 shows a spectral region centered at 290 nm where ionic states of Si and O begin to appear above the continuum. The lines are labeled by their degree of ionization and wavelength from Ref. 14. As the plume expanded further, the principal constituents of the line emissions derived from both neutral and singly ionized Si and O. In general, the plasma emission was attributed to electronic transitions in both Si^{+y} $(0\leqslant y\leqslant 3)$ and O^{+x} $(0\leqslant x\leqslant 3)$. Oxygen, however, did not appear as abundant as excited, ionic Si in the plume. Emission lines from both Si(V) and O(V) were also observed at early times and short distances, but these species were very short lived. No excited or ionized molecular species were observed during the course of this study.

Because of the transitory nature of laser-produced plasmas, the atomic and ionic populations present in the plume rapidly evolved with time and position. The sequence of spectral snapshots shown in Fig. 5 illustrates the temporal evolution of the plasma. Figures 5(a) and 5(b) show the behavior of the plasma at three delay times but fixed location from the target surface (5 mm) in two wavelength regions. The early time traces were dominated by highly ionized states of both Si and O ($+3$ and $+4$ degrees of ionization). Continuum emission was clearly visible as well. As the plasma evolved, emission from the $+3$ and $+4$ states subsided, and emission from electronically excited neutrals and $+1$ states prevailed for $t_d > 150$ ns. At very long delay times, only electronically excited neutral Si was observed. Linear plots of intensity versus time were generated from these temporal history records to quantify the temporal behavior of the excited species. Figure 6 shows examples of these plots. Summarizing the results, each ion state produced a characteristic intensity distribution which peaked at distinctive locations as detailed in Table I. Ion states up to and including $+3$ were observed as far as $z = 7.5$ mm. These distributions, however, decayed fairly rapidly unlike the lower ion states. As shown in Fig. 5, Si(I) was the sole surviving emitting species at long times.

Since the concentration of an electronic state is proportional to the area under its emission line (or the inten-

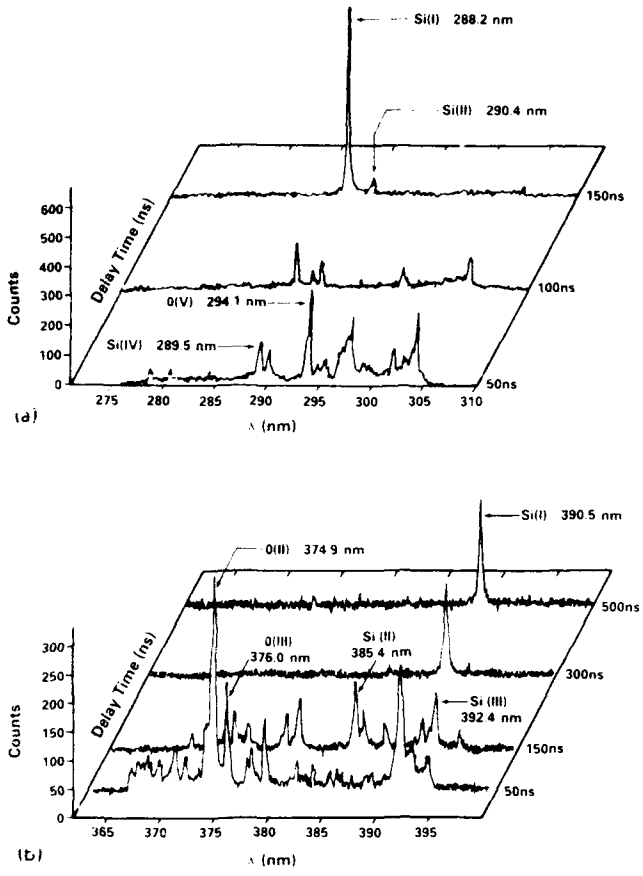

FIG. 5. The temporal evolution of the plasma's emission features recorded at $z = 5$ mm in two spectral regions centered at (a) $\lambda = 290$ nm and (b) $\lambda = 380$ nm. Continuum emission is clearly present at 50 ns but rapidly decays at $t_d = 100$ ns. The higher ionization states which appear at early times rapidly decay and they are replaced by emission from excited neutral and singly ionized atomic species as early as 150 ns from the incident laser pulse.

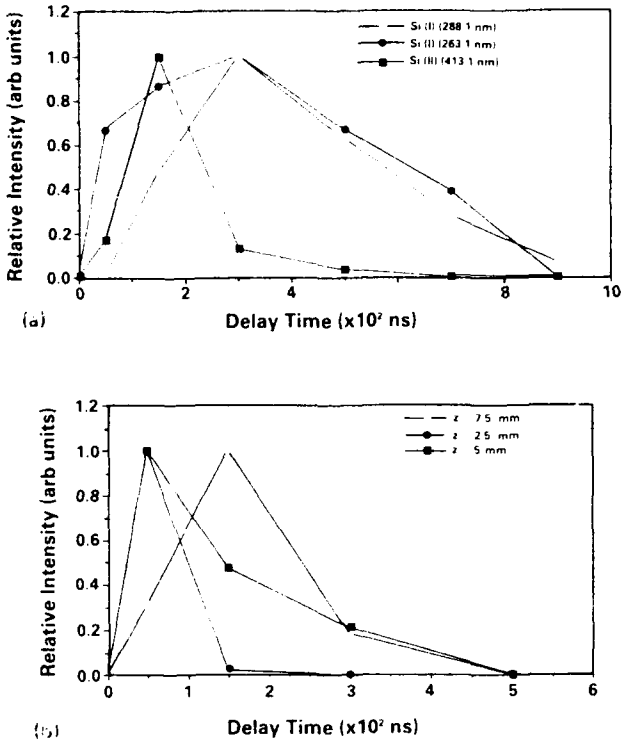

FIG. 6. The temporal history of Si species generated from spectra such as those shown in Fig. 5: (a) time profiles of S(I) and Si(II) at $z = 5$ mm; (b) time history of Si(III) recorded at three locations from the target surface.

sity), the plots of Fig. 5 can yield a time-of-flight behavior of various excited species in the plasma. Specifically, the information provided in Fig. 5 is useful for approximating the velocity of the plasma's leading edge. The distribution of Si(II) ions, based on the area under the 505.6 nm line as a function of time for two spatial locations (2.5 and 7.5 mm), is depicted in Fig. 7. At $z = 2.5$ mm, the peak of the distribution occurs at approximately 100 ns from the laser pulse while the distribution at $z = 7.5$ mm peaks in the vicinity of 300 ns. Based on the change in position of the leading edge position of the FWHM, the velocity is 2.5×10^6 cm s^{-1}. This velocity corresponds to a translational kinetic energy of 90 eV. In contrast, the flight time for the Si(I) using the 288.2 nm emission line is 1.4×10^6 cm s^{-1}, and the expansion velocity calculated from the O(II) data is approximately 4×10^6 cm s^{-1}, nearly a factor of 1.5 larger than the Si(II) expansion velocity.

B. Electron temperatures

If conditions in the plasma favor local thermodynamic equilibrium (LTE), the bound electrons are required to populate discrete energy levels according to the Boltzmann distribution.[13,15,16] In addition, the free electrons must obey the Maxwellian velocity distribution and the relative concentrations of two successive ion states must be governed by the Saha equation. Initially, the LTE approximation is assumed to be valid to extract both a temperature and an electron density, and this assumption will subsequently be explored for its validity. Since LPPs are transitory phenomena, LTE applies only to a fixed point and time in the

TABLE I. The locations and the corresponding times for the appearance of intensity maxima for various species in the plasma.

Species	Emission line (nm)	z (mm)	t (ns)
Si(I)	288.1	2.5	100
		5.0	300–400
		7.5	500
Si(II)	413.1	3.0	100
		5.0	150–200
		6.5	~250
Si(III)	392.4	2.5	50
		5.0	75
		7.5	100
O(III)	439.7	5.0	100
		6.5	150

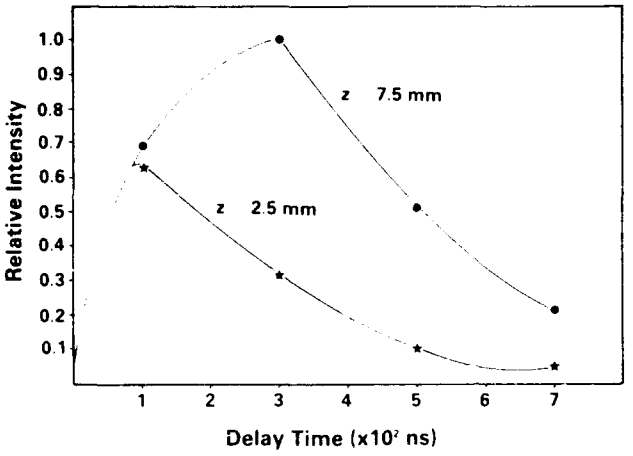

FIG. 7. The relative intensity of the 505.6 nm Si(II) emission line as a function of time recorded at two locations, $z = 2.5$ and 7.5 mm, from the target surface.

plasma development. Thus, the temperatures derived from the ensuing analyses should adequately define both the ionization and excitation states of the plasma at each location and time.

The relative line intensities from a particular ionization state measured along a line of sight are used to calculate the electron temperatures. The lines must be well resolved to obtain accurate intensities I_{mn} and the transition probabilities A_{mn} must be known. The prescription for determining the electron temperature is given by

$$\ln\left(\frac{I_{mn}\lambda_{mn}}{A_{mn}g_{mn}}\right) = \ln\left(\frac{N}{Z}\right) - \left(\frac{E_m}{kT_e}\right). \tag{1}$$

For a transition from an upper state m to a lower state n, λ_{mn} is the transition wavelength, E_m and g_m are the energy and degeneracy of the upper state, respectively, k is Boltzmann's constant, and T_e is the electron (ion) temperature. The temperature is obtained from the slope $(-1/kT_e)$ of the plot of the left-hand side of Eq. (1) versus E_m. The total number density N and the partition function Z are not required to determine the temperature.

The electron temperatures were determined using seven Si(II) emission lines in the doublet manifold. A partial energy-level diagram of Si(II) is shown in Fig. 8 for reference. The transition lifetimes, upper-level energies, and degeneracies were extracted from Ref. 17. Only the relative intensities (arbitrary units) were required for Eq. (1) and these values were obtained by integration of the OMA output with corrections for OMA-spectrometer sensitivity. A plot of Eq. (1) is shown in Fig. 9(a) for $z = 5$ mm and $t_d = 150$ ns which yielded a temperature of 3.0 eV. The data were fit with a least-squares approximation and the Boltzmann plots all had correlation coefficients exceeding 0.96. Table II summarizes the temperatures obtained from this procedure. The errors are 1σ from the mean and they correspond to errors in the reproducibility in the data.

Electron temperatures were also obtained from the emission lines originating from O(II). Figure 9(b) shows a representative Boltzmann plot for O(II) and a compilation

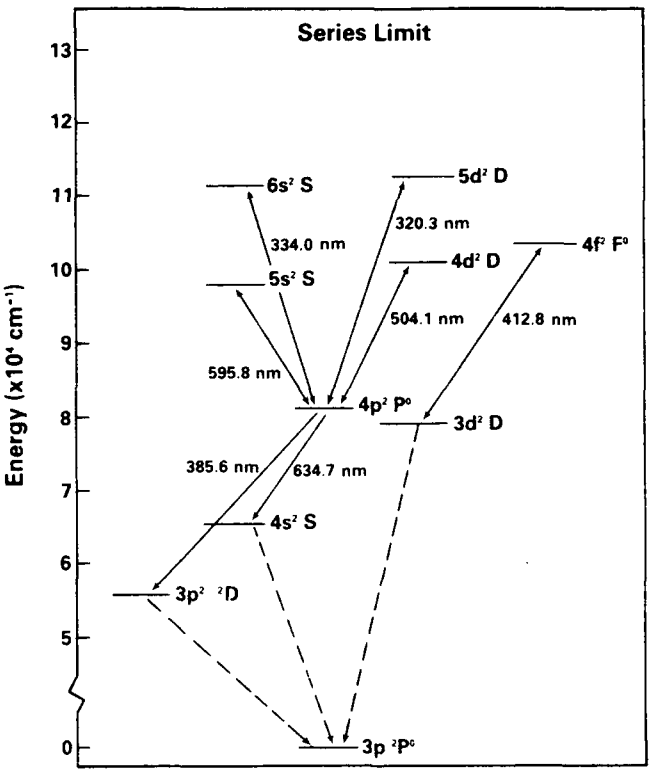

FIG. 8. A partial energy-level diagram of Si(II). The solid lines show the observed emission lines from the indicated electronic transitions. The dashed lines represent the unobserved, dipole-allowed transitions to the ground state.

of the O(II) temperatures are also provided in Table II. The errors for these values were considerably larger than for the temperatures determined from the Si(II) data because many O(II) lines overlapped other O^{+1} or Si^{+2} emission features which introduced error into the integration of the spectral features for determining the relative population. However, the temperature results from these ion states are consistent with those determined using the Si(II) emission lines.

C. Electron densities

The electrons in the plasma can perturb the energy levels of the individual ions which broaden the emission lines originating from these excited levels. Stark broadening of well-isolated lines in the plasma is, thus, useful for estimating electron number densities provided that the Stark-broadening coefficients have been measured or calculated.[13,15] Five lines of Si(II) were identified as candidates for electron-density measurements: 504.1, 595.7, 597.9, 634.7, and 637.1 nm. Figure 10 shows the 634.7 nm line with sufficient resolution to measure the FWHM (0.30 nm). All five lines showed approximately Lorentzian line shapes so the observed line shape was corrected by subtracting the contribution by instrumental line broadening using

$$\Delta\lambda_{\text{true}} = \Delta\lambda_{\text{observed}} - \Delta\lambda_{\text{instrument}}, \tag{2}$$

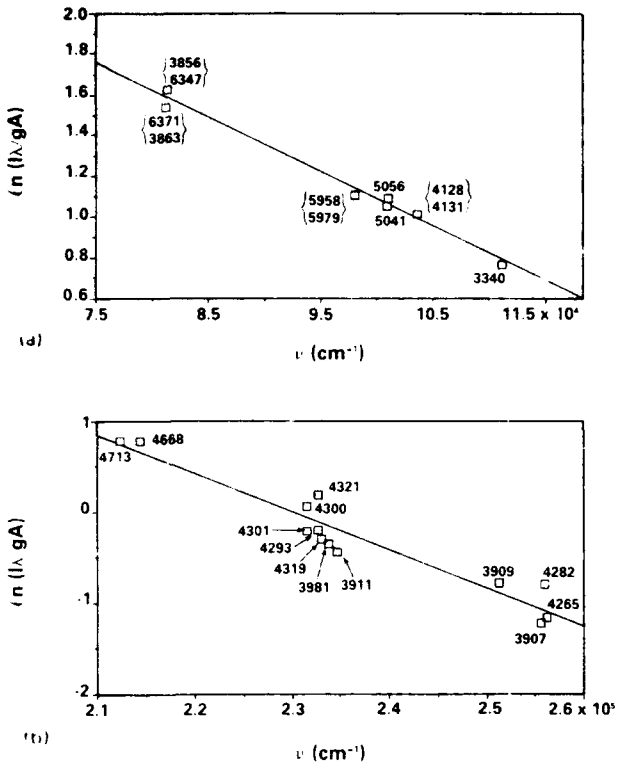

FIG. 9. Boltzmann plots for determining the electron temperatures: (a) Si(II) emission at $z = 5$ mm and $t_d = 150$ ns, and (b) O(II) emission at $z = 3$ mm and $t_d = 100$ ns. The Si(II) temperature was 3.4 eV from the slope of (a) and the data in (b) produced a temperature of 3.0 eV. The specific emission lines are labeled in angstroms next to the data points.

where $\Delta\lambda$ is the full width at half-maximum. Table III summarizes the parameters for the five emission lines for the specific case $z = 5$ mm and $t_d = 150$ ns.

For neutral and singly ionized atoms, the full width at half-maximum, $\Delta\lambda$, is given by[13]

$$\Delta\lambda = 2W\left(\frac{N_e}{10^{16}}\right) + 3.5A\left(\frac{N_e}{10^{16}}\right)^{1/4} \cdot \left[1 - \frac{3}{4}N_D\right]^{-1/3} W\left(\frac{N_e}{10^{16}}\right), \quad (3)$$

TABLE II. Summary of electron temperatures for Si(II) and O(II) at various spatial and temporal positions. The electron densities determined from the Stark-broadened linewidths of Si(II) emission lines are listed in the last column.

Species	z (mm)	t_d (ns)	T (eV)	N_e ($\times 10^{17}$ cm^{-3})
Si(II)	2.5	150	4.4 ± 1.3	1.4 ± 0.5
	5.0	150	3.4 ± 0.9	0.8 ± 0.2
	5.0	250	2.2 ± 0.7	0.7 ± 0.2
	6.5	250	3.4 ± 1.0	1.2 ± 0.5
	7.5	300	2.9 ± 0.9	1.0 ± 0.3
O(II)	5.0	150	3.8 ± 1.1	
	5.0	100	3.5 ± 1.4	
	3.0	50	3.5 ± 1.5	
	3.0	100	3.0 ± 1.4	

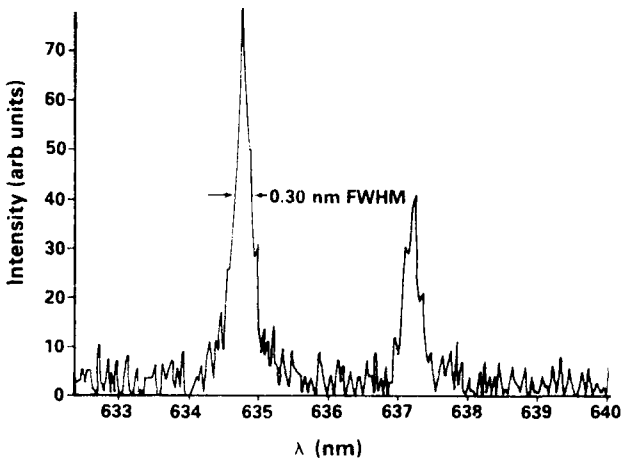

FIG. 10. The 634.7 nm emission line from Si(II) at $z = 5$ mm and $t_d = 150$ ns. The FWHM linewidth (0.30 nm) was used for determining the electron density via Stark broadening.

where the width is in Å and the electron density N_e is in cm^{-3}. The coefficients W and A, both independent of density and slowly varying with temperature, are the electron-impact width parameter and the ion-broadening parameter, respectively. The parameter N_D is the number of particles in the Debye sphere as given by

$$N_D = 1.72\times 10^9 \frac{T(\text{eV})^{3/2}}{N_e(\text{cm}^{-3})^{1/2}}. \quad (4)$$

The broadening coefficients W and A were interpolated at the appropriate temperatures from the values in Ref. 15. The contribution from ion broadening was small, typically less than 0.03 nm for the conditions of this experiment, so the width was mainly due to electron-impact broadening. The results of the number density calculations from the Stark-broadened linewidths for $z = 5$ mm and $t_d = 150$ ns are listed in the last column of Table III. The values range from 5.7×10^{16} to 9.5×10^{16} cm^{-3} with an average value of 7.6×10^{16} cm^{-3}.

As a check on the validity of the approximation used to calculate N_e, the particle density in the Debye sphere was calculated for the temperatures and densities determined in this study. The number of particles in the Debye

TABLE III. Parameters for electron-density calculations and the computed electron densities for Si(II) at $z = 5$ mm and $t_d = 150$ ns.

Emission line (nm)	W[a] at $T = 3.4$ eV and $N_e = 10^{16}$ cm^{-3} ($\times 10^{-3}$ nm)	A[a] at $T = 3.4$ eV ($\times 10^{-2}$)	N_e ($\times 10^{16}$ cm^{-3})
504.1	8.74	4.0	8.1
595.7	9.50	3.2	8.1
597.9	9.50	3.2	5.7
634.7	5.24	2.9	9.5
637.1	5.24	2.9	6.4
AVERAGE VALUE			7.6

[a]Interpolated from data in Ref. 15.

sphere was approximately 38 with $T=3.4$ eV and $N_e=8\times10^{16}$ cm^{-3}. This value of N_D was well above the lower limit ($N_D=2$) of the Debye approximation for correlation effects. The Doppler-broadening width was also calculated to determine its contribution to the overall linewidth since this mechanism effectively competes with Stark broadening. Using the temperatures in Table III, the Doppler half-widths were typically less than 0.01 nm and are, thus, negligible.

The last column of Table II summarizes the number densities for each temperature as a function of distance from the target and time after the laser pulse. The values of N_e are only as accurate as the coefficients used in the calculations. Since the Stark-broadening coefficients listed in Ref. 15 are calculated values, the number density determinations are, at best, approximations. The errors quoted in the last column of Table III are primarily due to the error associated with the temperature determinations. The quoted error ($\approx30\%$) is essentially equal to the error associated with the approximation in using Eq. (4) ($\approx20\%$–30%).

D. Film formation

The homogeneity of the plasma is an important quantity when computing the plasma properties from hydrodynamic models and subsequently comparing the results to experiments. The ejected material from the SiO_2 target was collected on Si substrates to investigate the plume composition. A visual inspection of the film revealed an elliptical deposition pattern with a typical dimension of 2.5 and 3.5 cm across the minor and major axes, respectively for a target-substrate distance of 5.5 cm. (The off-axis target ablation was responsible for the elliptically shaped film pattern.) A rainbow color pattern was also observed on the substrate which indicated a thickness that varied across the film surface. The latter result was not unexpected since laser-deposited films exhibit roughly a $\cos^n\theta$ ($n=8$–12) distribution depending on the laser parameters, irradiated spot size, etc.[18] This thickness variation is a consequence of the forward-directed nature of the hydrodynamic expansion.[19] The films were approximately 1 μm thick at the center and the surface was extremely rough as shown in Fig. 11. Scanning electron micrographs also revealed a morphologically rough surface with "boulders" having a lateral dimension of about 1–2 μm. The large boulders were presumably due to matter exploding from the target and collected on the surface at times long compared to the deposition time of the vapor. The film deposition rate was, on the average, constant at 3.0 A/s regardless of the location from the target (5.5 or 3 cm) or the deposition time (60 or 45 min). The generation of particulates is a problematic feature of laser-deposited films.[9] Higher particulate densities are usually formed under conditions that produce practical deposition rates ($0.1 < r < 10$ A/s) and under power densities where desirable energetic species are generated.

In the energy-resolved mode, the SEM identified the film as oxygen and silicon with a Si-to-O ratio of 1:2 which is consistent with an SiO_2 film composition. However, a

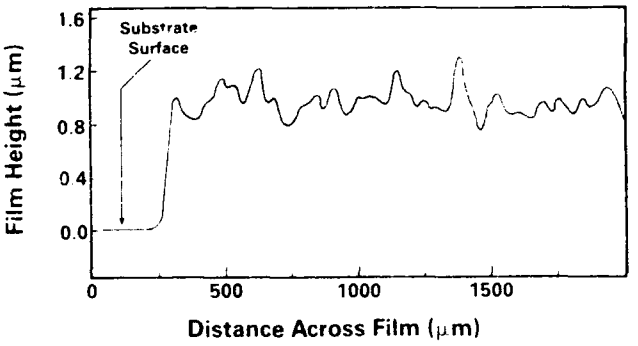

FIG. 11. Surface profiler measurement of the film thickness and substrate roughness. The substrate-target distance was 3 cm and the deposition time was 45 min. The rms roughness was approximately 230 nm.

more useful analysis of the films was performed using IR transmission spectroscopy. The films were deposited on NaCl substrates so IR transmission spectra could be recorded for these analyses. Figure 12 shows a sample IR spectrum of the deposited film. The group frequency for the Si-O stretching mode resides between 800 and 1100 cm^{-1}.[1,20] Thus, the absorption features appearing at 1055 and 805 cm^{-1} are attributed to Si-O stretching frequencies. The distinct feature at 3000 cm^{-1} is probably due to OH from adsorbed water on the substrate. (IR spectra on a bare substrate shows the same feature at 3000 cm^{-1}.)

These IR transmission results can be compared to thermally grown SiO and SiO_2 layers which have IR absorption peaks at 980 and 1090 cm^{-1}, respectively. Generally, the half-width and the position of the Si-O stretching modes near 1090 and 805 cm^{-1} are known to be strongly influenced by the bonding character, stoichiometry, density, and porosity of the films.[21,22] A decrease in density and an increase in both oxygen deficiency and bond strain will broaden and shift the 1090 cm^{-1} absorption feature to lower frequencies.[23] The strong absorption feature shown in Fig. 12 at 1055 cm^{-1} is certainly shorter in frequency than pure SiO_2 and longer than the Si-O stretching mode in SiO. This prominent absorption band also has a broader half-bandwidth (120 cm^{-1}) than the Si-O mode

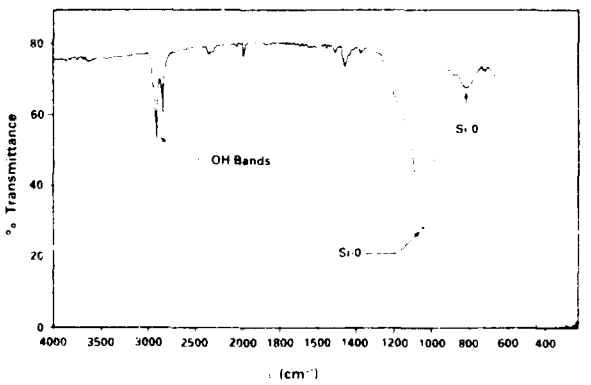

FIG. 12. Infrared transmission spectrum of a film formed on a NaCl substrate from laser ablation of a SiO_2 target. The absorption maximum at 1055 cm^{-1} is due to Si-O-Si stretching.

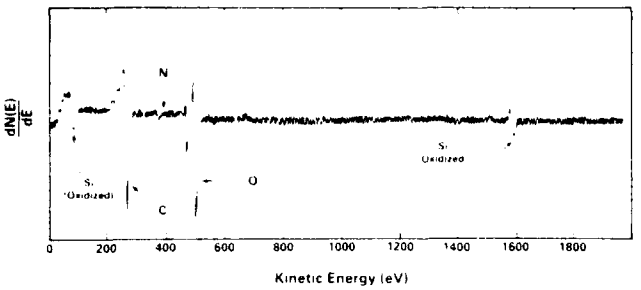

FIG. 13. Auger spectrum of a film formed on a Si substrate using an electron energy of 5 keV. Oxidized Si peaks are clearly visible in the spectrum.

in thermally grown SiO_2 ($\Delta\nu = 90$ cm^{-1}). This result implies that the atomic arrangement is more irregular than that in thermally grown silicon dioxide although the exact cause of the shift and broadening cannot be determined from IR spectroscopy alone. The IR spectra recorded in this study appear similar to those for chemical-vapor-deposited SiO_2 films.[24] The IR spectra do suggest, however, that the laser-deposited films are more characteristic of SiO_2 structure as opposed to SiO, although some intermediate SiO_x ($1 < x < 2$) structure could exist.[20,25]

The results of two additional film diagnostic tests appear to corroborate the results mentioned above. First, IR reflectance measurements (performed on films gathered on Si substrates) generated a strong reflectance peak at 1080 cm^{-1} (Si-O-Si stretching mode) and a weak absorbance peak near 680 cm^{-1} (Si-O-Si bending mode). These experimental IR features were interpreted with the aid of a computed IR reflectance spectra for SiO_2 and SiO. The optical constants from Ref. 26 provided the data for the computations. The calculated spectra showed a broad reflectance feature between 1300 and 900 cm^{-1} which peaked at 1100 cm^{-1}. In contrast, the SiO reflectance profile reached its maximum value near 980 cm^{-1}. Therefore, the experimental data indicates that the film stoichiometry is closer to SiO_2.

Finally, Fig. 13 illustrates the Auger spectrum of one film sample. The spectra presents the peaks associated with Si at approximately 80 and 160 eV and O at 500 eV. These peaks are near those for Si (LMM) from SiO_2 at 76 eV and O(KLL) at 512 eV. The C(KLL) peak at 270 eV is also present and is probably due to contamination in the Auger spectrometer. Unoxidized Si at 92 eV was not observed within the resolution of the spectra. These results again suggest a film composition that is nearer to SiO_2 rather than SiO.

IV. DISCUSSION

The local thermodynamic equilibrium assumption is used frequently to obtain quantitative information from plasmas. However, collisions must dominate the other energy-transfer processes (viz. radiative decay and recombination) to establish a Boltzmann distribution among the bound energy levels to assure the validity of the LTE approximation. In a partially ionized gas, electron collisions will be the dominant energy-transfer mechanism because of their high velocities and long-range Coulomb interaction. In order for electron collisions to maintain the populations of the atomic and ionic excited states, the electron density, N_e, must satisfy McWhirter's necessary condition[27]

$$N_e(\text{cm}^{-3}) \geq 1.6\times 10^{12} T^{1/2} (\Delta E)^3, \tag{5}$$

where T is the temperature in K. In Eq. (5), N_e is the lower limit for the electron density needed to collisionally maintain the energy-level populations to within 10% of LTE while competing with radiative decay. The term ΔE is the energy difference between the upper and lower states for which Eq. (5) is least likely to be satisfied. These energy states usually involve resonance levels whose populations are nearly always established by radiative processes. In this study, the largest experimentally observed energy gap between strongly coupled states is between the $5d\ ^2D$ and $4p\ ^2P^0$ electronic levels at 320.3 nm (see Fig. 8). Using $\Delta E = 3.9$ eV and a representative temperature of 3 eV, the lower limit given by Eq. (5) is 1.7×10^{16} cm^{-3}. The value of N_e estimated from the Stark-broadened lines is approximately a factor of 10 greater than the value calculated from Eq. (5). Thus, this result, coupled with the linearity of the Boltzmann plots as seen in Fig. 9, supports the validity of the LTE assumption.

Two additional factors must be considered to assure that the quantitative spectroscopy performed in this study is free from interpretive error. The first item is inverse bremsstrahlung absorption.[10] This phenomena occurs when the laser light is absorbed by an electron near an ion which can cause direct plasma heating by the laser. The inverse bremsstrahlung absorption coefficient can be estimated using

$$K_\nu = 3.69\times 10^{8} (Z^3 N_e^2 / T^{1/2} \nu^3), \tag{6}$$

where losses by stimulated emission are ignored. In Eq. (6), Z is the atomic number, N_e is the electron number density in cm^{-3}, T is the temperature in K, and ν is the frequency of the laser light. At $N_e = 1\times 10^{17}$ cm^{-3}, $\lambda = 1064$ nm ($\nu = 2.8\times 10^{14}$ s^{-1}), and $T = 3$ eV (3.5×10^4 K), Eq. (6) yields $K_\nu = 4.95\times 10^{-2}$ cm^{-1}. Since the plasma dimensions are a few millimeters (near the target surface where inverse bremsstrahlung would most likely occur), the weak absorption ($1/K_\nu = 81$ cm) does not affect the results.

Absorption of radiation within the plasma modifies the population densities of the energy levels which, in turn, alters the interpretation of the observed emission lines. In this experiment, the analyses of the emission spectra assumed that no self-absorption of the line radiation occurred from the emitting species. So, to check the validity of this assumption, the optical depth of the plasma must be evaluated.[10,28] For a homogeneous plasma, the optical transparency τ can be estimated using

$$\tau = 0.1668 f N d L(\omega) = K_\nu d, \tag{7}$$

where f is the absorption oscillator strength, N is the number density in the lower energy level, d is the length of the emitting layer, $L(\omega)$ is the normalized line shape for the

transition, and K_ν is the absorption coefficient per cm. The optical depth was estimated using the strongest observed transition in Si(II) at 634.7 nm ($4p\,^2P^0-4s\,^2S$) where $f=0.84$ and $L(\omega)\approx 1.06\times 10^{-12}$. The line-shape factor was estimated from the Lorentzian profile of the emission feature [$L(\omega)\approx 1/\Delta\omega$] with a corrected linewidth $\Delta\lambda=0.2$ nm. The number density in the $4s\,^2S$ state must now be estimated in order to determine the absorption coefficient.

The Saha equation describes the ratio of the number densities for two consecutive ionization stages for a locally equilibrated plasma. Using the measured values of the electron temperature and the number density at 5 mm from the target and $t_d=150$ ns ($T=3.4$ eV and $N_e=1\times 10^{17}$ cm^{-3}), the Saha equation predicts the following relative silicon concentrations: Si(II)/Si(I) $\approx$2000, Si(III)/Si(II) $\approx$450, and Si(III)/Si(IV) $\approx$1.9. The partition functions and the lowering of the ionization energy were determined from the data in Ref. 29, and the ionization energies used in the calculations were: Si(I) = 8.15 eV, Si(II) = 16.35 eV, and Si(III) = 33.46 eV.

These ratios can now be used to estimate the number density in the $4s\,^2S$ state in which absorption will occur. Equating the electron number density to the sum of the concentrations in Si(II), Si(III), and Si(IV) with the macroscopic neutrality condition,

$$N_e=\sum_{z,i} zN_i^z, \tag{8}$$

where z is the charge and N_i^z is the number density of species i in the zth ionization stage, the solution for the total Si(II) concentration is 1.1×10^{14} cm^{-3}. Using the Boltzmann equation and the number density for Si(II), the population in the $4s\,^2S$ state is approximately 6.8×10^{11} cm^{-3}. Thus, the estimated absorption coefficient for the 634.7 nm transition is 0.092 cm^{-1} and the optical depth d is 10.9 cm for $\tau=1$ ($1/e$ reduction in the intensity of the transmitted emission line). In this worst-case estimate, the optical depth is large compared to the estimated few millimeter plasma dimension. This analysis indicates that self-absorption does not appear to be important.

The semi-quantitative discussion presented above argues in favor of LTE and, thus, the plasma generated from a SiO_2 target using a laser flux of 7×10^{10} W cm^{-2} at 1.06 μm produced a temperature of 3–4 eV and an electron density of about 10^{17} cm^{-3}. However, the LTE approximation must break down at some temporal and/or spatial location in the plasma expansion. This will occur when the radiative rate of the electronically excited ions effectively competes with the electron-ion collisions. With typical radiative rates of about 10^9 s^{-1}, the electron number density must approach 10^{16} cm^{-3} (assuming a gas kinetic electron-ion collision rate constant of 10^{-9} cm^3 s^{-1}) in order to reach the LTE limit. This limit can be attained at approximately 10 mm from the target surface where other techniques must be employed to determine the plasma conditions. Sankur *et al.*[5] investigated the plasma generated by CO_2 irradiation of a SiO_2 target at $\phi > 10^8$ W cm^{-2}. They reported LTE temperatures near 6700 K which were measured close to the target surface. They also observed no (emitting) molecular species and ionization states up to Si^{+2}. These results are consistent with those obtained in the present study. The temperatures obtained here are about four to five times higher than those reported in Ref. 5 which is primarily due to the two orders of magnitude difference in the laser flux. The corresponding ionization stages should also be restricted in the low-flux case as was observed. Unfortunately, no electron number densities or species trends were reported in the CO_2 ablation studies.

The experimental data clearly show that electronically excited, neutral Si is the only remaining emitting species at both long times from the laser pulse and large distances from the target. As the plasma expands to the region of free molecular flow, the electron collisions may not be able to maintain the population equilibrium in the ion states. The ionic species will subsequently decay to their respective ground states due to their short lifetimes. The natural decay of these species is even more pronounced when growing thin films since substrate-target distances are usually an order of magnitude larger than the length of the high-density region in the plasma. While the atomic species will not reach the substrate in their ionically excited states, many ions and possibly metastable and excited metastable species will converge on the substrate with high electron and kinetic energies. In this study, the computed translational energy is approximately 90 eV which will affect the film growth. In fact, 10 °C temperature rises were typically recorded on the substrate holder which clearly indicated that excess heat was imparted to the film growth surface. The high particle energies could also have adverse affects. Defects could easily be created in the film surface and increased sputter rates may occur during the deposition. The 90 eV translational energy of the plasma is sufficient to sputter the substrate since the bond dissociation energy of (gaseous) Si_2 is only 3.1 eV. Unfortunately, there is insufficient data from this study to judge the effects of this excess energy on the film growing process.

The deduced expansion velocities for O(II), Si(I), and Si(II) were 4×10^6 cm s^{-1}, 1.4×10^6 cm s^{-1}, and 2.5×10^6 cm s^{-1}, respectively. The ratio of these velocities are remarkably similar to those obtained by Hanabusha, Moriyama, and Kikuchi[30] in their study on the dynamics of reactive sputtering to form Si films. Hanabusha and coworkers measured the flight speeds of Si(I), Si(II), and Si(III), and they found these velocities to be in the ratio 1:2:3. In this study, the ratio of velocities appears in the same proportion for the Si species. Furthermore, the O(II) speed is 1.5 times faster than that for Si(II) which is due to the lighter mass for O (mass of Si/mass of O = 1.8). Borrowing Hanabusha and co-worker's interpretation, local fields present in the plasma may cause the ions to accelerate, resulting in higher velocities as compared to neutral species.

These results may have import for growing thin films and understanding nucleation dynamics. The differing velocities imply that the higher ionization states of the lightest species will arrive at the substrate surface ahead of the species with lower ionization states and masses. In this work, $O^{+y}(y>1)$ may reach the substrate first, followed

by the various ion states of Si. At this point in these studies, it is not clear what affect selective ion bombardment has on the film growth of dielectric materials.

V. CONCLUSIONS

Energetic plasmas were generated from 1.06 μm irradiation of SiO_2 targets at a laser flux of 7×10^{10} W cm^{-2}. The ablated material was composed of several ion states of O and Si with typical temperatures of 3–4 eV and a translational energy of approximately 90 eV. The electron number density was also estimated to be 10^{17} electrons cm^{-3}. The temperature and the electron number density determinations depended strongly on the applicability of local thermodynamic equilibrium and arguments were presented that established the validity of this assumption. The material in the plume was collected on Si substrates and it was apparent that the blowoff consisted of both atomic vapor and particulates. These particulates severely contaminated the surface of the film. The film's composition, through IR and Auger analyses, suggested a stoichiometry of SiO_x ($1 < x < 2$). The results of this study also demonstrated that dielectric thin films can be formed under adverse conditions with approximately the same composition as the target and that film properties can be correlated with specific plasma conditions. The experimental apparatus is being modified to include additional diagnostics for detecting neutral atoms and molecules, and a time-of-flight mass spectrometer is being incorporated for a more detailed analyses of the film deposition process.

ACKNOWLEDGMENTS

I am in debt to the following individuals for their aid in performing specialized experiments and data analyses so this work can be completed: Dr. K. Rachocki, Department of Chemistry, USAF Academy, for obtaining the Auger spectra of the films, Dr. T. Deaton for his computational effort in predicting the IR reflectance spectra, and Mr. H. Ward for his technical help in the early stages of this work.

[1] T. T. Cheung and H. Sankur, CRC Crit. Rev. Solid State Mater. Sci. **15**, 63 (1988).
[2] A. Richter, Thin Solid Films **188**, 275 (1990).
[3] R. Messier, A. P. Giri, and R. A. Roy, J. Vac. Sci. Technol. A **2**, 500 (1984).
[4] A. W. Johnson, D. J. Ehrlich, and H. R. Schlossberg, Mater. Res. Soc. Symp. Proc. **29**, 373 (1984).
[5] H. Sankur, J. G. Nelson, A. T. Pritt, Jr., and W. J. Gunning, J. Vac. Sci. Technol. A **5**, 15 (1987).
[6] H. Wang, A. P. Salzberg, and B. R. Weiner, Appl. Phys. Lett. **59**, 935 (1991).
[7] H. Izumi, K. Ohata, T. Sawada, T. Morishita, and S. Tanaka, Appl. Phys. Lett. **59**, 597 (1991).
[8] R. K. Singh, O. W. Holland, and J. Narayan, J. Appl. Phys. **68**, 233 (1990).
[9] H. Sankur and J. T. Cheung, Appl. Phys. A **47**, 271 (1988).
[10] J. T. Ready, *Effects of High Power Laser Radiation* (Academic, New York, 1971).
[11] V. M. Donnley, Mater. Res. Soc. Symp. Proc. **68**, 95 (1986).
[12] K. Niemax and W. Sdorra, Appl. Opt. **29**, 5000 (1990).
[13] George Befeki, in *Principles of Laser Plasmas*, edited by G. Befeki (Wiley Interscience, New York, 1976).
[14] J. Reader, C. H. Cross, W. L. Wiese, and O. A. Martin, *Wavelength and Transition Probabilities for Atoms and Atomic Ions*, National Standard Reference System—NBS 68 (U.S. Government Printing Office, Washington, DC, 1980).
[15] H. R. Griem, *Plasma Spectroscopy* (McGraw-Hill, New York, 1964).
[16] J. Richter, in *Plasma Diagnostics*, edited by W. Lochte-Holtgreven (Wiley Interscience, New York, 1968).
[17] W. L. Wiese, M. W. Smith, and B. M. Miles, *Atomic Transition Probabilities*, Vol. II, *Sodium Through Calcium (A Critical Data Compilation)*, National Standard Reference Data System—NBS-22 (U.S. Government Printing Office, Washington, DC, 1969); W. L. Wise, M. W. Smith, and B. M. Glennon, *Atomic Transition Probabilities*, Vol. I, *Hydrogen Through Neon (A Critical Data Compilation)*, National Standard Reference Data System—NBS-4 (U.S. Government Printing Office, Washington, DC, 1966).
[18] R. A. Neifeld, S. Gunapala, C. Liang, S. A. Shaheim, M. Croft, J. Price, D. Simons, and W. T. Hill, III, Appl. Phys. Lett. **53**, 703 (1988).
[19] S. Witanachchi, H. S. Kwok, X. W. Wang, and D. T. Shaw, Appl. Phys. Lett. **53**, 234 (1988).
[20] Kazuo Nakamoto, *Infrared and Raman Spectra of Inorganic and Coordination Compounds* (Wiley Interscience, New York, 1986).
[21] W. A. Pliskin and H. S. Lehman, J. Electrochem. Soc. **112**, 1013 (1965).
[22] G. Hass and C. D. Salzberg, J. Opt. Soc. Am. **44**, 181 (1954).
[23] W. A. Pliskin, J. Vac. Sci. Technol. **14**, 1064 (1977).
[24] J. Wong, J. Electron. Mater. **5**, 113 (1976).
[25] E. Fogarassy, C. Fuchs, A. Slaoui, and J. P. Stoquert, Appl. Phys. Lett. **57**, 664 (1990).
[26] H. Philipp, in *Handbook of Optical Constants of Solids*, edited by Edward D. Palik (Academic, New York, 1985), pp. 719–769.
[27] R. W. P. McWhirter, in *Plasma Diagnostic Techniques*, edited by R. H. Huddlestone and S. L. Leonard (Academic, New York, 1965).
[28] W. Lochte-Holtzgreven, in *Plasma Diagnostics*, edited by W. Lochte-Holtzgreven (Wiley, New York, 1965), p. 135.
[29] H. W. Drawin and P. Felenbok, *Data for Plasmas in Local Thermodynamic Equilibrium* (Gauthier-Villars, Paris, 1965).
[30] M. Hanabusha, S. Moriyama, and H. Kikuchi, Thin Solid Films **107**, 227 (1983).